ARTICLE   OPEN

Check for updates

Thermodynamics of multi-sublattice battery active materials: from an extended regular solution theory to a phase-field model of LiMn$_y$Fe$_{1-y}$PO$_4$

Pierfrancesco Ombrini [1], Martin Z. Bazant [2,3], Marnix Wagemaker[1] and Alexandros Vasileiadis[1]✉

Phase separation during the lithiation of redox-active materials is a critical factor affecting battery performance, including energy density, charging rates, and cycle life. Accurate physical descriptions of these materials are necessary for understanding underlying lithiation mechanisms, performance limitations, and optimizing energy storage devices. This work presents an extended regular solution model that captures mutual interactions between sublattices of multi-sublattice battery materials, typically synthesized by metal substitution. We apply the model to phospho-olivine materials and demonstrate its quantitative accuracy in predicting the composition-dependent redox shift of the plateaus of LiMn$_y$Fe$_{1-y}$PO$_4$ (LFMP), LiCo$_y$Fe$_{1-y}$PO$_4$ (LFCP), LiCo$_x$Mn$_y$Fe$_{1-x-y}$PO$_4$ (LFMCP), as well as their phase separation behavior. Furthermore, we develop a phase-field model of LFMP that consistently matches experimental data and identifies LiMn$_{0.4}$Fe$_{0.6}$PO$_4$ as a superior composition that favors a solid solution phase transition, making it ideal for high-power applications.

INTRODUCTION

Li-ion batteries are fundamental to the upcoming transition toward sustainable energy production, electric mobility, and energy storage[1]. Although the early storage requirements were satisfied by active materials such as graphite and LiCoO$_2$[2,3], higher energy densities, sustainability, cheaper elements, and improved safety require developing more sophisticated battery active materials. Li-ion battery electrode materials also have other emerging applications[4], such as electrochromic displays[5], ion-tunable electrocatalysis[6], resistive switching memory[7–9], water desalination and purification[10], and lithium extraction from brines[11,12]. In all of these applications, the design space for electrode materials with various desired properties has hardly been explored.

Blending or modifying existing electrode materials is a promising method to improve properties, which is gaining attention, albeit with limited theoretical guidance. While the anode materials are moving toward silicon[13], silicon/graphite composites, or Li-metal[14], cathode development is running behind, with most advancements focusing on substituting cobalt in layered oxide materials with Ni, Mn, or Al developing LiNi$_x$Mn$_y$Co$_{1-x-y}$O$_2$ (NMC) and LiNi$_x$Al$_y$Co$_{1-x-y}$O$_2$ (NCA) cathodes[15,16]. These approaches show the advantages of modifying the composition of an existing cathode with well-established lithiation mechanisms to reduce its cost and environmental impact and to improve energy density and cycle life. Applying the same approach to LiFePO$_4$ (LFP), a phospho-olivine material introduced by Goodenough and co-workers in 1997[17], which has advantages over the layered oxides in lower cost and toxicity with greater stability and recyclability[18], various partial or complete substitutions of Fe with Mn, Co, and Ni have been attempted. Higher redox potential and similar specific capacities can be obtained, improving the overall energy density[19–21] while sustaining decent

diffusivity and cycle life. Currently, LiMn$_y$Fe$_{1-y}$PO$_4$ (LFMP)[21–23] exhibits the most promising characteristics and is rapidly being incorporated into commercial batteries. Therefore, it is crucial to gain a deep understanding of the basic physics of LFMP through modeling. Other materials in the same family, such as LiCo$_y$Fe$_{1-y}$PO$_4$ (LFCP)[24–29] and LiCo$_x$Mn$_y$Fe$_{1-x-y}$PO$_4$ (LFMCP)[19,20,30], also display intriguing properties and merit further investigation as well.

First-principles calculations struggle to provide a complete picture of the underlying mechanisms, in part due to the heavy impact of the practical choice of the pseudopotentials on the predicted redox potential[31,32] and partly because the use of Monte Carlo simulations aided by cluster expansion[33] prevent the understanding of the behavior of the material in a realistic battery system at finite temperature.

Mesoscale modeling, based on mean-field theories of electrochemical nonequilibrium thermodynamics[34], is instead a suitable tool to investigate the effects of different chemistries, morphologies, and cycling strategies in Li-ion batteries due to its low computational costs and flexibility. Different models have been developed depending on the goal and the required precision[35–39]. Progress has been made in modeling phase-separating active materials regarding single particle behavior[40–46] and collective dynamics in a battery environment[35,47–54].

In order to develop an accurate thermodynamic description, it was essential to model the behavior of individual particles using phase-field methods, which generalize the Cahn-Hilliard formalism[55–61] for driven electrochemical systems[34,48,52]. This approach has led to realistic models of diffusion and reaction models for materials such as graphite[62,63], anatase TiO$_2$[45], LTO[46], LCO[9] and LFP[64–68], showing excellent agreement with experiments, guiding researchers to properly understand the reasons for various peculiar behaviors occurring in phase-separating materials and

[1]Storage of Electrochemical Energy, Department of Radiation Science and Technology, Faculty of Applied Sciences, Delft University of Technology, Mekelweg 15, 2929JB Delft, The Netherlands. [2]Department of Chemical Engineering Massachusetts Institute of Technology, Cambridge, MA 02139, USA. [3]Department of Mathematics, Massachusetts Institute of Technology, Cambridge, MA 02139, USA. ✉email: a.vasileiadis@tudelft.nl

helping companies in the optimization of these kinds of batteries. Recently, phase-field modeling of LFP has succeeded in reproducing a vast dataset of *operando* x-ray images of nanoparticles cycling at different rates pixel by pixel[69], while learning the two-phase free-energy landscape, the reaction kinetics of coupled ion-electron transfer[70], and the heterogeneity of surface reactivity, correlated with variations in carbon coating thickness. An open-source code, MPET (Multiphase Porous Electrode Theory)[48] has been developed to facilitate the implementation of these models for specific cells and control algorithms[71]. With its modular design, users can quickly incorporate phase-field models of the studied material within a porous electrode theory framework, providing insights into both the individual particle and the collective system responses.

In this study, we applied a thermodynamic-based approach to investigate the impact of composition on the performance of phospho-olivine materials. We extended the regular-solution theory[61,72], originally applied to single-lattice LFP[34,73], to consider the presence of multiple sublattices for the intercalated species, which have distinct properties and redox potentials. Our theory reveals how interactions between sublattices explain the composition dependence on redox potential and phase transition behavior. By applying the theory to a phase-field simulation of an LFMP half-cell, we gain fundamental insights into the optimal transition metal ratio, which demonstrate the possibility of using mean-field phase-field models to design active materials.

RESULTS

Multi-sublattice regular solution theory

The mathematical modeling of a closed thermodynamic system starts by defining the Helmholtz free energy F, given by $F = E - TS$[61,72]. To determine the properties of a solid solution, we need the temperature T, a function for the entropy S, linked to all possible configurations the system can have, and the internal energy E, representing interactions between the particles of the system. The regular solution model, which is equivalent to a mean-field lattice-gas model with pair interactions, offers an elegant and straightforward way to describe solid solutions, and it was implemented successfully in various battery active materials[34,40,44–46,48,63,73]. However, its application is mainly limited to materials where the intercalated species encounter one lattice type, such as LFP or LTO[46], or two non-interacting sublattices, such as TiO_2[45]. Phase-field models of staging phase transitions in graphite have been developed with multiple, periodic interacting crystal layers[40], but the parameters must be fitted to experimental data to describe the complex phase diagram of the material[62,63,74].

To summarize this mean-field theory, we can start considering an active material containing N lattice sites that can host intercalating species (e.g., lithium) whose relative concentration is defined as $\widetilde{c} = N_{occupied}/N$. The entropy $S = -k_B N[\widetilde{c}\ln(\widetilde{c}) + (1-\widetilde{c})\ln(1-\widetilde{c})]$, where κ_B is the Boltzmann constant, is derived from the possible configurations of the intercalated system, and the internal energy $E = Nz\left[\frac{1}{2}\varepsilon_{oo}\widetilde{c} + \frac{1}{2}\varepsilon_{vv}(1-\widetilde{c}) + \frac{\Omega}{z}\widetilde{c}(1-\widetilde{c})\right]$ is obtained considering only pair interaction energies, ε_{oo}, ε_{vv}, ε_{vo} between two occupied sites, two vacancies, or a vacancy and an occupied site, respectively[61]. These are then multiplied by the number of atoms and the number of closest neighbors z. To apply the model is therefore not necessary to know all the interaction energies, but it is sufficient to know $\Omega = z(\varepsilon_{vo} - \frac{1}{2}\varepsilon_{oo} - \frac{1}{2}\varepsilon_{vv})$, which represents the mixing enthalpy, determining whether the material will favor phase separation during (de)intercalation. In the context of rechargeable battery materials, the absolute value of the energy carries no physical meaning, while the difference between the completely intercalated state and the empty state provides the standard chemical potential $\mu^{\Theta} = \frac{(E(\widetilde{c}=1)-E(\widetilde{c}=0))}{N}$.

The standard chemical potential can so be associated with the interaction energies, $\mu^{\Theta} = z\left(\frac{\varepsilon_{oo}}{2} - \frac{\varepsilon_{vv}}{2}\right)$, and the total energy can be rewritten as $E = N\left[\Omega\widetilde{c}(1-\widetilde{c}) + \mu^{\Theta}\widetilde{c}\right]$. A connection is so established between the approximation governing the regular solution theory and the redox potential as intrinsic physical property of the material. The regular solution theory finally provides the occupation-dependent chemical potential of the intercalated materials as $\mu(\widetilde{c}) = \frac{1}{N}\frac{\partial F}{\partial \widetilde{c}} = k_B T \ln\frac{\widetilde{c}}{1-\widetilde{c}} + \Omega(1-2\widetilde{c}) + \mu^{\Theta}$.

One way to obtain the parameters introduced above is by performing first-principles calculations, attaining the energies of the structure at different fractions of intercalation, and subsequently determining the mixing energy and the redox potential[75]. Moreover, it is possible to measure the chemical potential experimentally during close-to-equilibrium (de)intercalation; fitting the voltage hysteresis gap will then capture the difference between the local minima and maxima of the Ω dependent chemical potential[44,76].

A practical example of the application of this model is $LiFePO_4$, in which for every intercalated Li-ion, an adjacent Fe is reduced from Fe^{3+} to Fe^{2+} so that an occupied site consists of an ensemble of Li^+, Fe^{2+}, and PO_4, forming what is approximated as a neutral specie, while a vacancy consists of Fe^{3+}, PO_4 and an empty lattice position. The standard chemical potential is then usually redefined with respect to the redox potential of the redox reaction Li metal - Li^+.

Aiming to describe a general multi-sublattice material in which the lattice sites are mixed uniformly, the usual regular solution model must be modified to account for the various interactions that the intercalated species can have in the material.

We consider a lattice composed of N intercalating sites, divided into n sublattices, of which $N_i = y_i N$ belong to the sublattice i. Assuming that the lattice sites of different types are fixed in space after the synthesis of the entropy for the sublattice i, having an occupation $\widetilde{c}_i = N_{occupied_i}/N_i$, is calculated using the solid solution approach, resulting in

$$S = -\sum_{i=1}^{n} k_B N_i[\widetilde{c}_i\ln(\widetilde{c}_i) + (1-\widetilde{c}_i)\ln(1-\widetilde{c}_i)] \quad (1)$$

The internal energy of the general system with n different sublattices E is computed using a mean-field pair interaction approach so that the effect of the sublattices interactions arises naturally.

Using the same logic behind the regular solution model, we can start considering a scheme represented in Fig. 1, in which, for clarity, only two types of sites are considered. It shows how an intercalated particle in the occupied lattice site i will interact with other occupied sites of type i, the vacancies of the sites i, but also with the vacancies and the occupied sites of type j, leading to 9 different interaction energies for a 2-sublattice material.

The evaluation of the interaction energies between different sites ε_{ij}, in such complex systems, is challenging and would involve atomistic quantum mechanical computations. As a first approximation, we calculate them as an average between the same-site interactions $\varepsilon_{ij} = (\varepsilon_{ii} + \varepsilon_{jj})/2$.

Assuming that the site-site interactions ε_{ij} are not influenced by the ratio between the compounds y_i, the total internal energy will so be obtained considering that an atom or a vacancy in the sublattice i, having z close neighbors, will interact with $z_i = y_i z$ neighbors with an energy ε_{ooii}, ε_{vvii} or ε_{voii} depending on their occupation state, but also with $z_j = y_j z$ neighbors with an energy ε_{ooij}, ε_{vvij} or ε_{voij}. Applying this concept and considering all the
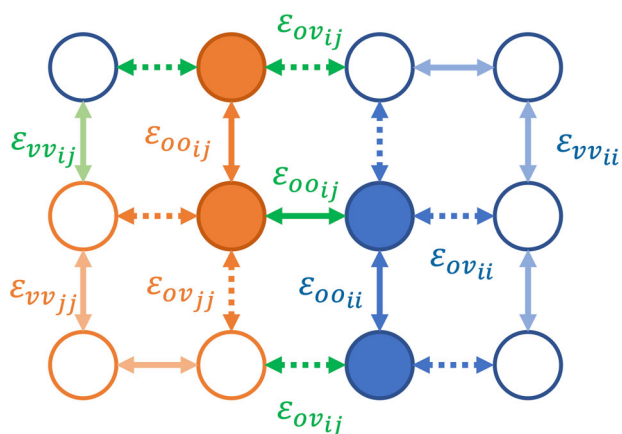
Fig. 1 Schematic representation of the interaction of a 2-sublattice material according to the extended regular solution model. The empty and full circles indicate vacancies and occupied sites, respectively. The species in the sublattice "i" (blue) interact with themselves through interaction energies $\varepsilon_{oo_{ii}}, \varepsilon_{ov_{ii}}, \varepsilon_{vv_{ii}}$ (full dark blue arrow, dotted blue arrow, full light blue arrow). Same for the species in the sublattice "j" (orange) $\varepsilon_{oo_{jj}}, \varepsilon_{ov_{jj}}, \varepsilon_{vv_{jj}}$ (full dark orange arrow, dotted orange arrow, full light orange arrow). The intra-sublattice interactions are represented in green: $\varepsilon_{oo_{ij}}, \varepsilon_{ov_{ij}}, \varepsilon_{vv_{ij}}$ (full dark green arrow, dotted green arrow, full light green arrow). The squared crystal structure and number of interactions of each type are for visual intent, not representative of the physics of the system.

possible combinations, the internal energy is

$$E = \sum_{i=1}^{n}\sum_{j=1}^{n} \frac{N_i z_j}{2}\left[\varepsilon_{oo_{ij}}\left(\frac{\widetilde{c}_i + \widetilde{c}_j}{2}\right) + \varepsilon_{vv_{ij}}\left(1 - \frac{\widetilde{c}_i + \widetilde{c}_j}{2}\right) + \frac{\Omega_{ij}}{z}\left(\widetilde{c}_i + \widetilde{c}_j - 2\widetilde{c}_i\widetilde{c}_j\right)\right]$$

(2)

Where Ω_{ij} can be calculated as

$$\Omega_{ij} = \frac{(\Omega_{ii} + \Omega_{jj})}{2}$$

(3)

and it will coincide with $\Omega_{ii} = z\left(\varepsilon_{vo_{ii}} - \frac{1}{2}\varepsilon_{oo_{ii}} - \frac{1}{2}\varepsilon_{vv_{ii}}\right)$, the value for the single lattice structure where only one kind of interaction is present. A complete derivation of Eq. (2) is presented in the section 1.1 of the supplementary information.

Equation (2) links the properties of the original materials, which are summarized in $\Omega_{ii}, \Omega_{jj}, \dots, \Omega_{nn}$, to the properties of the mixed compound. We can thus conclude that this one equation describes the system in all its possible compositions, becoming a powerful tool for alloy engineering.

Distinguishing now between the absolute energy dependence on concentration (first two terms in Eq. 2) and the enthalpy of mixing (last term in Eq. 2), the free energy of the system can be rewritten as

$$F = N\left\{\sum_{i=1}^{n}\sum_{j=1}^{n} y_i y_j \Omega_{ij}\left(\frac{\widetilde{c}_i + \widetilde{c}_j}{2} - \widetilde{c}_i\widetilde{c}_j\right) + \sum_{i=1}^{n} y_i k_B T[\widetilde{c}_i \ln(\widetilde{c}_i) + (1-\widetilde{c}_i)\ln(1-\widetilde{c}_i)] + \sum_{i=1}^{n} y_i \widetilde{c}_i \mu_i^{\ominus}\right\}$$

(4)

Where $\mu_i^{\ominus}$ is the standard chemical potential for the sublattice i, which is related, as described above, to the standard half-cell potential of the reacting sublattice $V_i^{\ominus}$, and conserve the intrinsic physical property of the redox potential for the specific sublattice.

Once the regular solution theory has been reformulated for a multi-sublattice active material, it is crucial to analyze the analytical solution to gain insight into the impact of various alloying elements on the material's behavior before obtaining the free energy functional needed to construct a comprehensive phase-field model.

To predict the behavior of the system is necessary to build an n dimensional energy space and follow the concentration path that

minimizes the energy extracted to transform the system from a completely deintercalated state, where $\widetilde{c}_1, \widetilde{c}_2, \dots \widetilde{c}_n = 0$, to a fully occupied system where $\widetilde{c}_1, \widetilde{c}_2, \dots \widetilde{c}_n = 1$. In this way, it is possible to numerically obtain a solution for $F(\widetilde{c})$, and from it, a voltage curve for a homogenous single particle system can be obtained $V(\widetilde{c})$.

If the difference in standard chemical potential between the lattice sites is significant compared to Ω_{ij} we will observe a series of redox plateaus in the voltage curve. Conversely, a more complicated energy path will be followed (see supplementary information, section 2.1). Limiting ourselves to the first case, we can analytically calculate the chemical potential, and so the voltage curve of the various plateaus as

$$\mu_i = \frac{1}{y_i N}\frac{\partial F}{\partial \widetilde{c}_i}$$

(5)

$$\mu_i = k_B T \ln\left(\frac{\widetilde{c}_i}{1 - \widetilde{c}_i}\right) + \sum_{j=1}^{n} y_j \Omega_{ij}(1 - 2\widetilde{c}_j) + \mu_i^{\ominus}$$

(6)

This simple formulation allows us to analytically capture how the system behaves depending on the compositions $y_i, y_j, \dots, y_n$ and the known factors $\Omega_{ii}, \Omega_{jj}, \dots, \Omega_{nn}$.

In fact, considering an intercalation process, we can deduce that in case $\mu_1^{\ominus} < \mu_{2,3,\dots}^{\ominus}$ the intercalated species will initially sit in the lattice sites here defined as "1" keeping $\widetilde{c}_{2,3,\dots} = 0$, and then, once $\widetilde{c}_1 \sim 1$ the second lattice sites will react, and so on. Therefore, the effective standard chemical potentials measured will be

$$\mu_{1_{eff}}^{\ominus} = \mu_1^{\ominus} + \sum_{j=2}^{n} y_j \Omega_{1j}$$

(7)

From Eq. (7), we can conclude that, due to the enthalpic contributions of the surrounding sublattices, the effective chemical potential, and so the measured redox potential $V_i^{\ominus}$, will be decreased by a value corresponding to the sum of the pair mixing energy coefficients, weighted by their corresponding stoichiometry. For the second plateau, we instead expect that since $\widetilde{c}_1 \sim 1$ the redox potential will increase by a factor $y_1\Omega_{12}$ and be reduced by a factor $\sum_{i=3}^{n} y_i \Omega_{2i}$.

Moreover, it is worth noticing how the effective enthalpic interaction $\Omega_{i_{eff}} = y_i \Omega_{ii}$ is now a function of the stoichiometry of the compound. In the case of phase-separating materials, this will impact the voltage hysteresis gap and the overall phase separation behavior with respect to the pure original lattice. Knowing that if $\Omega_{i_{eff}} < 2k_B T$ no phase separation will occur during the plateau of the specie "i", we can directly calculate the compositions that assure a solid-solution transition $y_{i_{ss}} < 2k_B T / \Omega_{ii}$ depending directly on temperature and the mixing energy of the original compound.

The theory can so be straightforwardly applied to intercalating electrode materials. Following the example of the phospho-olivine materials, a single sublattice position will be composed by the ensemble of an intercalated specie, a transition metal and the PO_4 tetrahedron. The stoichiometry of the transition metal "i" will thus correspond to y_i, while $\widetilde{c}_i$ indicates the fraction of transition metal which lattice spot is occupied.

Moreover, the presented theoretical structure can also be compared with the compound energy formalism (CEF)[77] of the CALPHAD approach to solution modeling[78]. Specifically, to develop the theory, we followed the point of view of intercalated atoms so that we defined a sublattice as a set of lattice positions composed of the inserted specie and the corresponding reduced transition metal. From another perspective, the system can be seen as a single lattice having $2n$ species: a vacancy and an occupied spot for each insertion site. In this context, Eq. (4) can be considered as an expression of the free energy, including the excess free energy, in terms of the site interactions within the
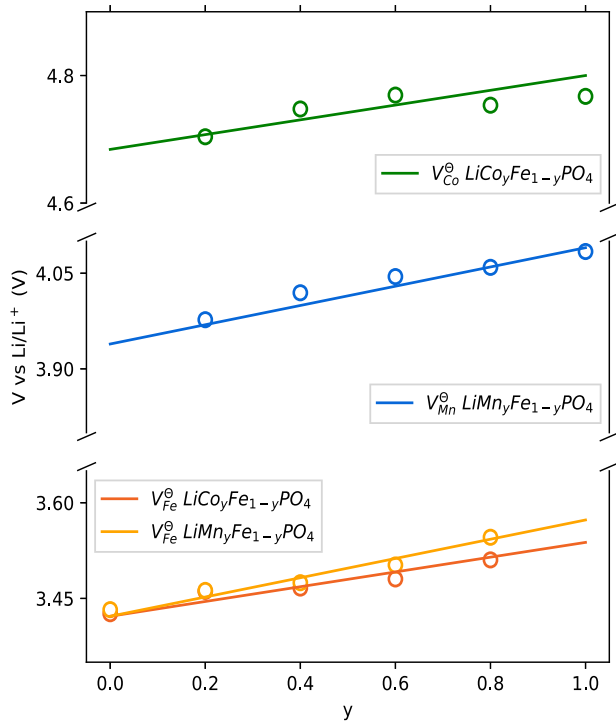
Fig. 2 Experimental vs. calculated redox potentials. Comparison between the calculated (lines) and the measured (empty dots) redox potential at various Mn and Co substitutions (y). The green line is the redox potential shift of the Co plateau in $LiCo_yFe_{1-y}PO_4$, while the dark orange is its counterpart in the Fe plateau. The blue line is the redox potential shift in $LiMn_yFe_{1-y}PO_4$, and the light orange one is the redox shift in the corresponding Fe plateau.

same sublattice, and Eq. (3) as a generalized approximated form of the bond energy model for multiple species[79]. Finally, it must be stated that we do not expect the obtained model to be able to predict the complete phase diagram since, differently from the CALPHAD approach, the parameters are directly taken from the regular solution model interpretation of electrochemical data rather than fitted to experimental phase diagrams. While for general solid compounds, the CALPHAD approach is feasible and necessary, its application to battery materials requires a wide set of experiments and strongly depends on the choice of the end-members model[80]. Our approach is instead applicable to electrochemical data making it more suitable for active material battery modeling.

Application to phospho-olivine cathodes

The available literature and the need for a reliable electrochemical model make phospho-olivine cathodes an excellent candidate for a critical verification of the developed theory by testing its implications on the redox potential shift and the order of the phase transition. We focus on the most promising iron substitutions in $LiFePO_4$ (LFP) by Mn and Co. Cyclic voltammetry and voltage curve data from the literature can provide the necessary information to implement in the model. For obtaining the enthalpies of mixing of the single sublattice of $LiFePO_4$ (Ω_{FeFe} in our multi-sublattice notation) and $\mu_{Fe}^{\ominus}$, we can rely on previous regular solution models for LFP were $\Omega_{FeFe} = 4.63 k_B T$ and $\mu_{Fe}^{\ominus} = -3.422 eV$ per Li atom. However, for $LiMnPO_4$ (LMP) and $LiCoPO_4$ (LCP), no previously developed models are available, so we must obtain $\Omega_{MnMn} = 7.44 k_B T$ and $\mu_{Mn}^{\ominus} = -4.09 eV$ per Li atom from fitting the voltage curve from Tasaduk et al.[20] and the cyclic voltammetry of Kobayashi et al.[81], respectively. Obtaining values for $LiCoPO_4$ presents particular challenges due to its instability

with the current electrolyte[24], limiting the available data. Nevertheless, we note that the peak separation of the cyclic voltammetry in the work of Jalkanen et al.[82] is close to that of LFP. Since the peak separation is proportional to the voltage gap due to phase separation, we can assume that $\Omega_{CoCo} \approx \Omega_{FeFe}$ and that $\mu_{Co}^{\ominus} = -4.78 eV$ per Li atom can be determined from the peak midpoint.

Starting by analyzing the shift in redox potential, we can compare the midpoints of the cyclic voltammetry results at different Fe substitutions from refs. [57,59] with the redox shift obtained from the theory. The expected dependence of the redox potential on the Mn content y for the plateaus in $LiMn_yFe_{1-y}PO_4$ will so be

$$V_{Mn_{eff}}^{\ominus} = V_{Mn}^{\ominus} + y\Omega_{FeMn}$$

$$V_{Fe_{eff}}^{\ominus} = V_{Fe}^{\ominus} - (1-y)\Omega_{FeMn}$$

Making the same calculations for the LFCP, we can see in Fig. 2 how the theory predicts the experimental values without any fitting parameters. A strong indication of the validity of the theory is in the quantitative prediction of the shift in the Fe plateau $\Delta V_{Fe}^{\ominus} = (y-1)\Omega_{FeX}$ which clearly does not depend on the original redox potential but only on the value of the average enthalpic interaction Ω_{FeX}, which is different for the case of Co and Mn substitution. For the $LiCoPO_4$ case, we could have been more precise by considering the double redox plateau present, seemingly linked to a staging behavior[28,29]. At present, we chose to neglect this effect, assuming it would pose minimal effect on the pair interaction energies, therefore, the chemical potential of LCP can be approximately modeled in the same fashion as that of LFP and LMP.

These results establish a strong foundation for the mean-field theory and offer a clear explanation for how the redox shift can be attributed to the interaction between surrounding lattice sites, in agreement with the Monte Carlo calculations of Malik et al.[33] in which the shift in redox potential was attributed to the effect of the pair interaction energies. It is remarkable that the straightforward assumption of averaging the two interaction energies, as demonstrated in Eq. 3, continues to hold true, even when the phenomenon is rooted in atomistic behavior.

Exploiting now the predictive capabilities of the model, in particular, the possibility of calculating the solid-solution compositions $y_{i_{ss}} < 2k_B T/\Omega_{ii}$, we can analyze the previously mentioned olivine phosphates, creating a ternary phase diagram (Fig. 3) revealing the order of phase transition (solid-solution or phase separation) for the corresponding plateau based on the compositions of $LiCo_xMn_yFe_{1-x-y}PO_4$. Explicitly considering the mixing energies described above, we calculate the solid-solution composition at ambient temperature of the Mn sublattice to be $y_{Mn_{ss}} = 0.26$, where for every other composition of Fe or Co, the particle transforms as a solid solution during the Mn plateau. Applying the same concept to Fe and Co, we obtain $y_{Co_{ss}} = y_{Fe_{ss}} = 0.43$.

The predicted equilibrium phase transition behavior aligns with the available data in the literature. The experiments of Jalkanen[82] and Kobayashi[81] show the CV peak separation of the corresponding plateau to be linearly dependent on the composition of the olivine material. Further, the works of Ravnsbæk[83–85] and Strobridge[29] analyze the operando XRD profiles of different compositions of LFMP and LFCP, exposing the absence of phase separation for the corresponding sublattice if the composition is below the one calculated from the model.

Therefore, the mathematical theory and the associated phase diagram can become tools for the practical engineering of these alloys. For example, they enable the selection of a composition range in which the material behaves as a complete solid solution (red triangle), at least from an equilibrium thermodynamics
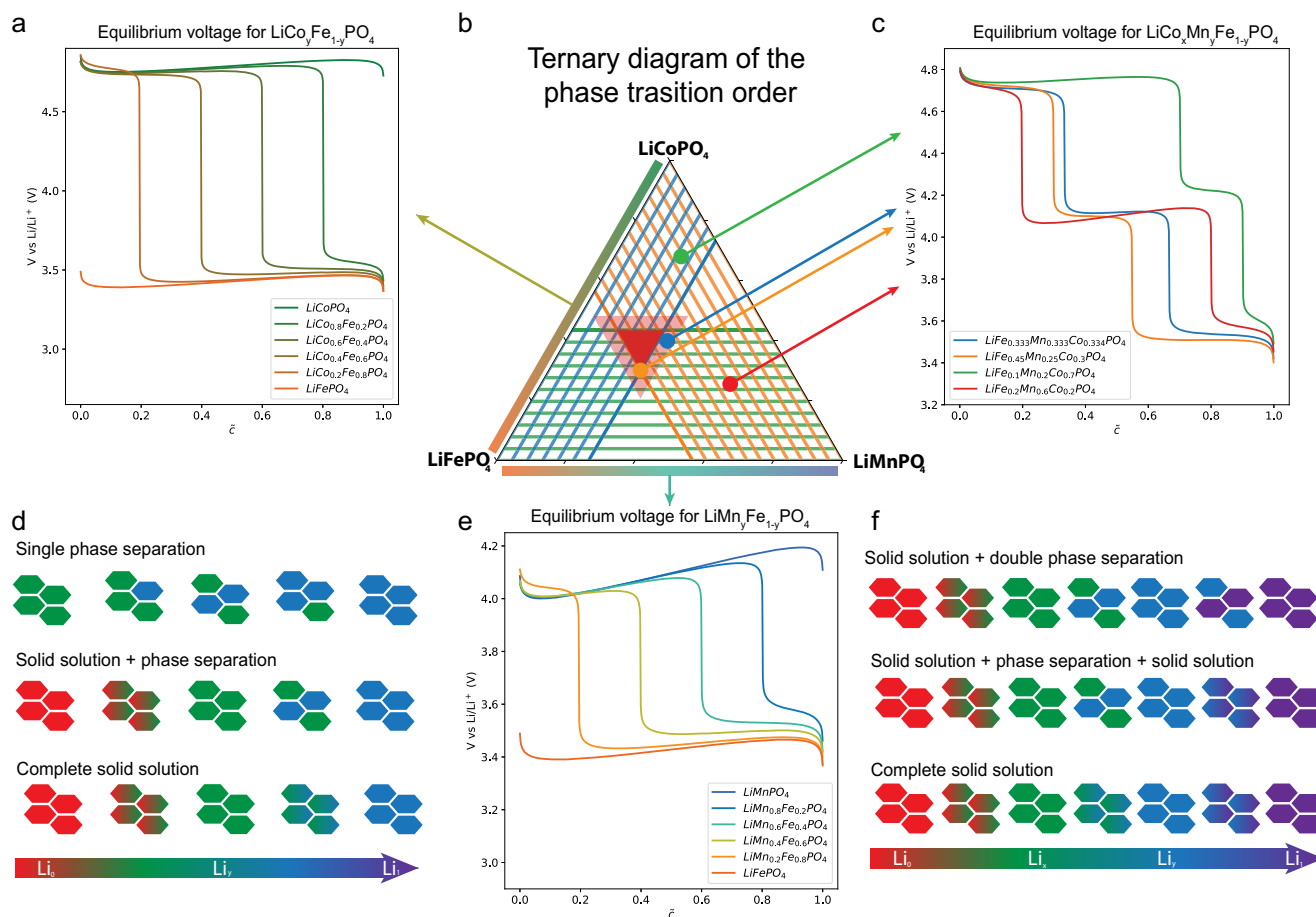
Fig. 3 Ternary phase transition diagram and corresponding voltage profiles. Voltage curves of LiMn$_y$Fe$_{1-y}$PO$_4$, LiCo$_y$Fe$_{1-y}$PO$_4$, LiCo$_x$Mn$_y$Fe$_{1-x-y}$PO$_4$ (**a**, **c**, **e**) originated from analytical calculations of the ternary phase transition diagram (**b**). The dark red zone indicates the compositions in which a thermodynamically consistent solid solution behavior is expected during the entire (de)lithiation. The light red zone is a qualitative extension indicating that the solid solution zone may be wider due to other stabilizing effects, such as coherency strain and lattice mismatch. Demonstration of the possible phase transition combinations (**d**, **f**) depending on the stoichiometry of the various metals.

perspective. We expect a wider zone (light red) in which the real system could behave as a solid solution due to the stabilizing effects of coherency strain[41], auto-inhibitory intercalation reactions[52], and the relation between the particle dimensions and the phase separation front[29,86]. To specifically characterize this wider zone a full phase-field model of each composition should be created. Within the solid solution region, it is also possible to select the composition that minimizes the Co content (orange curve for LFCMP in Fig. 3). The complete solid-solution behavior is confirmed by experiments on both LiMn$_{1/3}$Co$_{1/3}$Fe$_{1/3}$PO$_4$[30], and LiMn$_{0.3}$Co$_{0.2}$Fe$_{0.5}$PO$_4$[87] in which the systems show a monotonically decreasing voltage curve.

These conclusions come directly from the analytic application of the extended regular solution theory and the consistent calculations of Ω_{Fe}, Ω_{Mn} and Ω_{Co} without the need for ab-initio simulations. The mean-field model also helps in the phenomenological description of the system. The dilution of a sublattice, and its consequent reduction in first neighbors, weakens the attractive interaction between the intercalated atoms allowing the entropic contribution to take over, leading to a solid solution. Since this effect is subtle, a temperature change will also lead to different behavior (see supplementary information, section 2.2). This conclusion differs from the one reported by Malik et al.[33] in which the disappearance of the phase separation for certain

compositions was attributed to the reduction in the Li composition difference between the initial and the final state.

Finally, the combination of the predictions for the redox potential shift and the phase transition naturally leads to the possibility of calculating the voltage curves for every composition, including LFMP, LFCP, and LFMCP, in good accordance with the previously cited experimental results.

Phase field modeling

Having demonstrated a correspondence between experimental data and the analytical solution of the model, it is now interesting to investigate other factors that may come into play when the system is out of equilibrium. This can be accomplished by employing a complete phase-field simulation, which takes into account factors such as coherency strain and gradient penalties. Beginning with a simulation of a single particle, the behavior will be observed during both charging and discharging, with the aim of gaining insight into the collective dynamics that arise at various compositions.

Given the wealth of available experimental data in the literature and the potential for commercial applications[88], we have narrowed our focus to LFMP simulations. We implement our model in the open-source code MPET[48], freely available in its GitHub repository. The complete set of equations and the
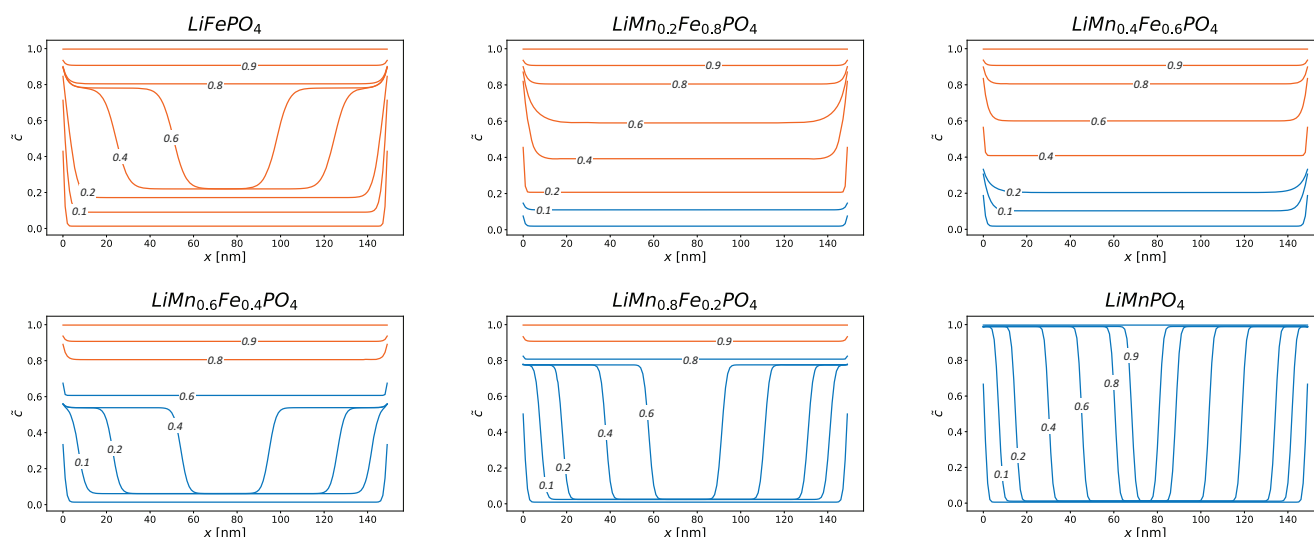
Fig. 4 Evolution of the normalized Li concentration inside a 150 nm particle upon lithiation. The blue lines correspond to the Mn plateau, the orange lines to the Fe plateau. The labels show the average composition of the particle.

parameters of the phase-field simulations can be found in section 1.2, 1.3 of the supplementary information, alongside a comparison of the simulated and measured voltage curves at equilibrium (section 2.3).

Single particle simulations

The single particle simulations in equilibrium (C/1000) (Fig. 4) show how modifying the enthalpic contribution at different compositions affects the system. Given y the fraction of Mn in $LiMn_yFe_{1-y}PO_4$, for the cases of $y = 0.6$ and $y = 0.8$, we obtain $\Omega_{Fe_{eff}} < 2k_BT$ at ambient temperature so that the particle, as expected from the analytical calculations, behaves as a solid solution during the (de)intercalation of the Fe plateau and phase separate when in the Mn plateau. In contrast, for intermediate values of y within the range of 0.2–0.4, although the effective interaction energies $\Omega_{Fe_{eff}}$ and $\Omega_{Mn_{eff}}$ exceed the critical threshold of $2k_BT$ for phase separation, the coherency strain provides a stabilizing effect that leads to the transformation of the particle into a solid solution. The insertion direction in our one-dimensional model is the one in which the coherency strain is minimum, which coincides with the preferential direction for phase separation[41]. This implies that the observed solid-solution behavior will remain consistent when considering a three-dimensional particle.

This claim requires further experimental verification, keeping in mind that the composition where we experience suppression of the phase separation may slightly differ from the one observed in simulations due to the documented sensitivity of the calculated coherency strain values on ab-initio simulation parameters[89,90]. However, the single-particle simulations rationalize how the composition $LiMn_{0.4}Fe_{0.6}PO_4$ with its probable solid-solution behavior can limit the problems due to the measured low Li diffusivity[91].

Porous electrode simulations

We used our single-particle model in a multiparticle simulation in which the simulated particles are considered part of a porous electrode regulated by the porous electrode theory[43,48,92,93]. We can so include the electrolyte transport limitations, described by the Stefan-Maxwell concentrated electrolyte theory[48], obtaining a realistic representation of the distribution of the Li concentration along the depth of a cathode.

In particular, it is interesting to simulate the effect of the composition on the possible suppression of phase separation, already known for LFP, and on the lithium distribution along the depth.

We distinguish the phenomena by performing simulations at two different Mn content: the first consists of simulating the charge and discharge process of a thin electrode at C/10 to assess the collective dynamic, and the second involves a 1 C discharge of a thicker electrode to focus on the transport limitations. All the simulations are done on an ensemble of 400 particles with lognormal size distribution.

The computed evolution of the concentration during the C/10 cycle was collected in a probability distribution and converted to normalized volume expansion (see supplementary information, section 1.4) to better compare the result with the work of Ravnsbæk et al.[84]

The results, shown in Fig. 5, not only strongly agree with the work of Ravnsbæk et al.[84], but they also offer a thermodynamically consistent explanation of them. Both in experiments and simulations, a bimodal volume distribution is present in the plateaus where the theory predicts phase separation. Moreover, it is essential to state that, considering the cases of $LiMn_{0.2}Fe_{0.8}PO_4$ and $LiMn_{0.4}Fe_{0.6}PO_4$ where, as discussed in the previous paragraph, we predict a solid solution transition for the single particle, the collective dynamics are dominated by the non-monotonic shape of the chemical potential and its subsequent concentration-dependent exchange current density[52]. Since we are close to equilibrium conditions (C/10), we can conclude that the origin of this bimodal distribution is established by the inter-particle separation (mosaic lithiation) in which the smaller particles are more lithiated than, the bigger ones, as also observed for LFP[94].

Focusing on the asymmetry between charge and discharge, for $LiMn_{0.4}Fe_{0.6}PO_4$, both in simulations and experiments, the phase separation of the Fe plateau is present only during charging. From this observation, Ravnsbæk et al.[83] suggested that the intrinsic order of the phase transition in $LiMn_{0.4}Fe_{0.6}PO_4$ depends on the direction of the transition and attributed the reason to coherency strain effects. Our consistent thermodynamic model enables us to reinterpret these conclusions offering a physical explanation for the observed experimental behavior. Our simulations indicate the significance of the collective auto-inhibitory and auto-catalytic behavior upon lithiation and delithiation, respectively[52]. Due to the asymmetric concentration dependence of the exchange current density upon delithiation, an enhanced particle-by-
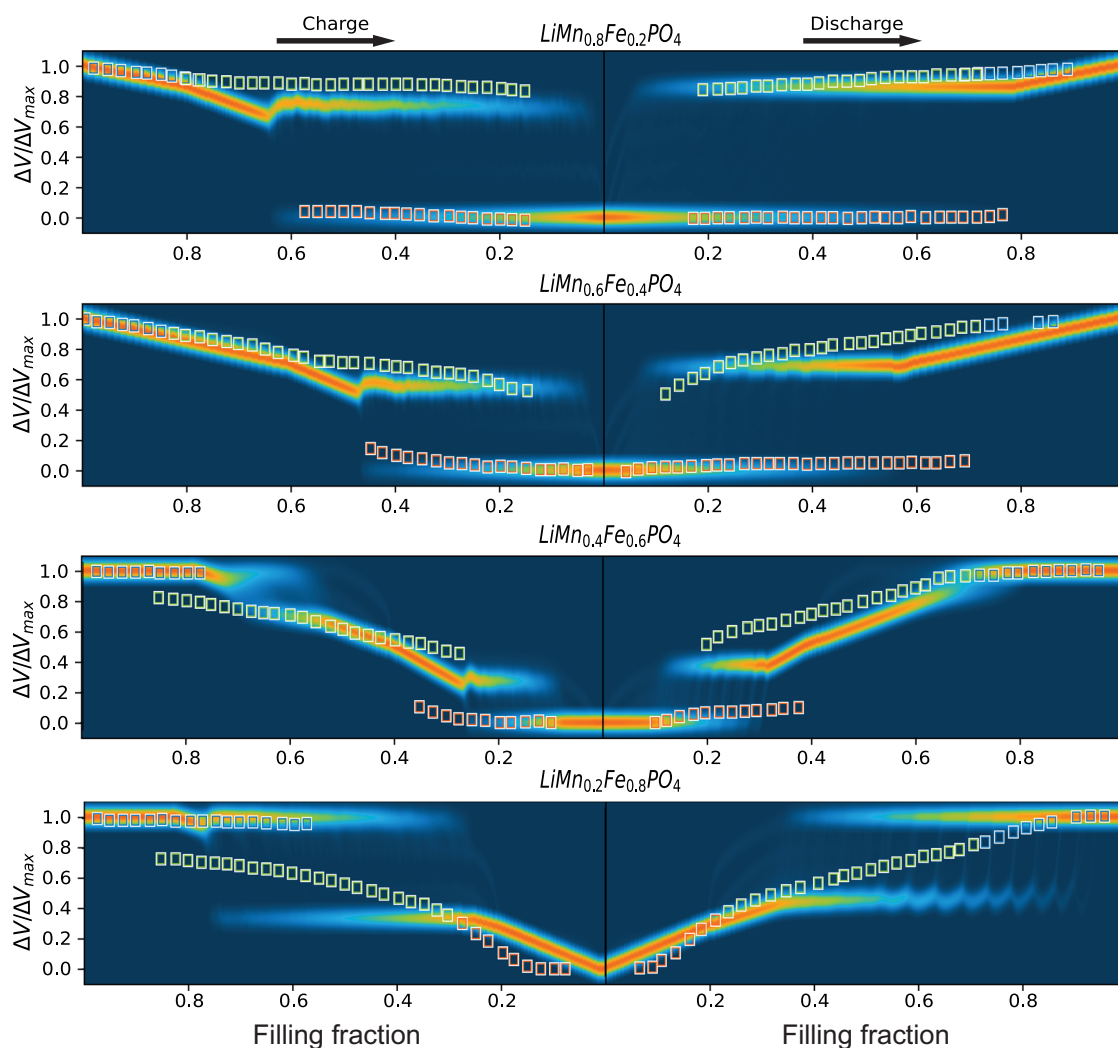
Fig. 5 Volume evolution for LiMn_yFe_1-yPO_4 during charge and discharge compared to experiments. The heatmaps represent the simulated probability of the normalized calculated volume evolving during a charge-discharge cycle at C/10 from fully lithiated ($\Delta V \backslash \Delta V_{max} = 1$) to fully delithiated ($\Delta V \backslash \Delta V_{max} = 0$). The simulated data are broadened, applying a Gaussian convolution for visual intent[54]. The empty squares are the experimental data points of the Rietveld refinement from the work of Ravnsbæk et al.[84].

particle reaction is observed, while during lithiation, the inter-particle separation is suppressed, as previously observed in LFP[93–101] and NMC[54] porous electrodes. While this phenomenon is only observed when cycling LFP at high rates, it is instead already present at C/10 in the Fe plateau of LFMP due to the low Ω_{Feeff}. The only observed mismatch in Fig. 5 occurs in the discharge case of LiMn_0.2Fe_0.8PO_4 and can be attributed to various phenomena not included in the model such as a possible metastable phase for the Fe plateau[102,103], effect of particle size[86,104] or non-linear dependence of the volume on the Li concentration.

Finally, it is expected that already at 1 C, in the case of a thin cathode, in the range $0.2 < y < 0.4$, the inter-particle separation is completely suppressed during lithiation (see supplementary information, section 2.5), even if low intra-particle diffusivity may lead to different experimental results.

To complete the picture, we studied the effect of the composition on the lithium depth profile during a 1 C discharge of a commercial-like cathode. The simulated half-cell has a cathode thickness of $80\,\mu m$ a porosity of 30%, the transport limitations of Li in the electrolyte are therefore not negligible anymore. Due to the absence of the nucleation barrier, solid solution materials tend to lithiate relatively uniformly along the

depth, even in the case of strong transport limitation. On the other hand, phase-separating materials show steeper gradients in the Li concentration[105,106]. The mixed phase separation—solid solution behavior of LFMP makes it an exciting candidate to evaluate this effect since the different compositions affect the phase transition. As shown in Fig. 6, if LiMn_0.8Fe_0.2PO_4 is used, the Mn plateau will show an inhomogeneous redox activity, typical of phase-separating materials, while the last 20% of the discharge, corresponding to the Fe plateau, will have a uniform reaction along the depth. Similar considerations can be made on LiMn_0.4Fe_0.6PO_4 in which a small but visible peak in redox activity can be seen in both plateaus due to the non-monotonicity of the chemical potential, which is still present even if the single particle is not phase separating.

We can so conclude that the Li distribution along the depth of the electrode at different states of charge is severely affected by the concentration of Mn. Taking LFP as a reference, it is clear that the change in the degree of phase separation helps guarantee uniform lithiation along the depth, and the case of LiMn_0.4Fe_0.6PO_4 is the one that most favors homogeneity. This result significantly impacts the cycle life, thanks to the possibility of reducing current hot spots, and offers a route for a composition-based optimization of a commercial electrode.
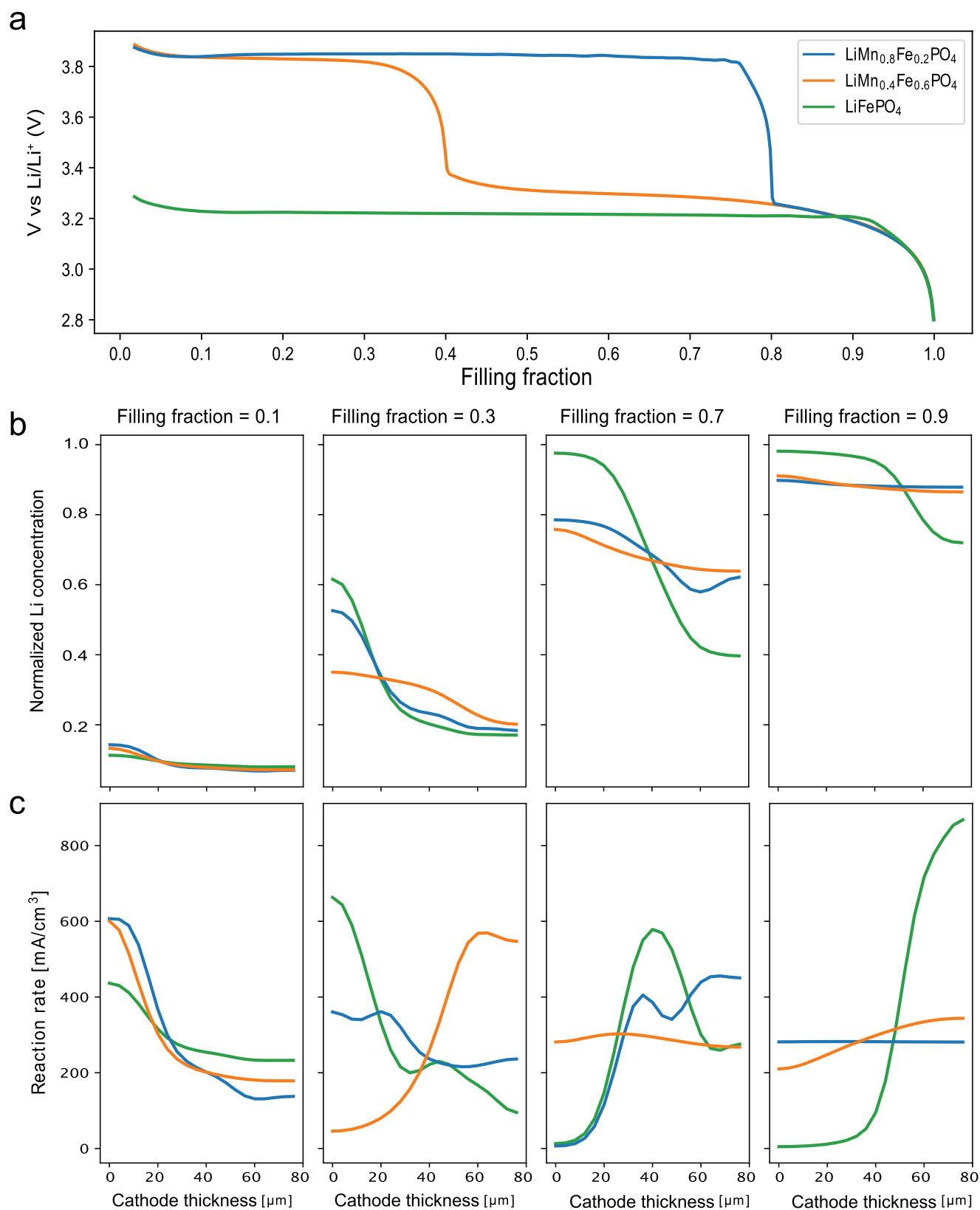
Fig. 6 Effect of composition on transport limitations. Voltage curves of a 1 C discharge of LiFePO$_4$, LiMn$_{0.4}$Fe$_{0.6}$PO$_4$, LiMn$_{0.8}$Fe$_{0.2}$PO$_4$ (**a**). Normalized Lithium concentration along the depth of the simulated cathodes at various states of the discharge (**b**), the separator is posed on the left side ($x = 0\mu m$), while the current collector is on the right ($x = 80\mu m$). Reaction rate along the depth of the simulated cathodes at various states of the discharge (**c**).

DISCUSSION

In this study, we expanded the regular solution theory to explain and predict the behavior of phospho-olivine cathodes. The inclusion of multiple sublattices and their interactions provided an elegant explanation for the shift in redox potential and phase separation behavior. The mean-field theory formalization offers an intuitive understanding of these phenomena, which can enable research on new active materials. This approach can serve as a valuable alternative to computationally extensive ab-initio calculations, delivering clear insights starting from simple concepts instead. Our phenomenological description of the mathematical derivation demonstrates that the redox shift is due to the interactions of the non-reacting sublattice. Furthermore, we found that a redox plateau that previously showed phase separation can transform into a solid solution. This transformation occurs due to the reduced number of closest neighbors within the same sublattice, which lowers the effective interactions of the intercalated species.

The application of our model to well-studied materials such as LFMP, LFCP, and LFMCP and their possible compositions shows how quantitative and accurate this theory is, even if the examined system is considered complex. The subsequent application in a phase-field framework was able to reproduce and explain various experimental results whose interpretations were incomplete and lacked mathematical support. The firm conclusion about the absence of phase separation in low Mn content LFMP is still to be confirmed experimentally. However, the proposed mechanism to explain the operando XRD peak shift sheds light on the importance of considering multi particles behavior when experimenting with a collective system such as a half-cell.

Finally, this model strongly indicates the optimal composition for a high-power cathode, showing how $LiMn_{0.4}Fe_{0.6}PO_4$ may be an excellent candidate thanks to its solid solution behavior and low transport-induced inhomogeneity. To verify this claim, further experiments are necessary, and a two-dimensional model, able to capture the known transport limitation in the particle, is also advised. The interplay between the concentrations of the two sublattices may play an essential role in explaining the out-of-equilibrium behavior opening the route for optimization of the (dis)charging procedure to exploit these effects[107]. We expect that the presented theory may be applied to other popular active materials such as $LiMn_{1.5}Ni_{0.5}O_4$ (LMNO) or the various compositions of NMC, explaining the effect of metal ratios on the performances. To do so, it will be necessary to consider the structural modifications occurring in the spinel or the layered structure that, at the moment, are not taken into account in the theory. It is finally hoped that overcoming these limitations may expand the domain of this theory in such a way that, as particle dimension, porosity, and thickness, also the composition of the materials can be included in the parameters to optimize when a battery is designed, improving cycle life and energy efficiency.

DATA AVAILABILITY

The open-source nature of the code also makes it possible to reproduce the described simulations using the parameters described in Supplementary Table 1 of the method section of the supplementary information.

CODE AVAILABILITY

MPET is available as a Bitbucket repository: https://bitbucketorg/mpet/src/master/, but at the moment, it does not contain the LFMP model in the master branch. The reader is thus invited to visit the GitHub repository of the code to explore the different branches: https://github.com/TRI-AMDD/mpet.git.

REFERENCES

1. Goodenough, J. B. & Park, K.-S. The Li-Ion Rechargeable Battery: A Perspective. *J. Am. Chem. Soc.* **135**, 1167–1176 (2013).
2. Zhang, H., Yang, Y., Ren, D., Wang, L. & He, X. Graphite as anode materials: Fundamental mechanism, recent progress and advances. *Energy Storage Mater.* **36**, 147–170 (2021).
3. Lyu, Y. et al. An Overview on the Advances of $LiCoO_2$ Cathodes for Lithium-Ion Batteries. *Adv. Energy Mater.* **11**, 2000982 (2021).
4. Sood, A. et al. Electrochemical ion insertion from the atomic to the device scale. *Nat. Rev. Mater.* **6**, 847–867 (2021).
5. Rauh, R. D. Electrochromic windows: an overview. *Electrochim. Acta* **44**, 3165–3176 (1999).
6. Wang, H. et al. Direct and continuous strain control of catalysts with tunable battery electrode materials. *Science* **354**, 1031–1036 (2016).
7. Gonzalez-Rosillo, J. C. et al. Lithium-Battery Anode Gains Additional Functionality for Neuromorphic Computing through Metal–Insulator Phase Separation. *Adv. Mater.* **32**, 1907465 (2020).
8. Tian, H. & Bazant, M. Z. Interfacial Resistive Switching by Multiphase Polarization in Ion-Intercalation Nanofilms. *Nano Lett.* **22**, 5866–5873 (2022).
9. Nadkarni, N., Zhou, T., Fraggedakis, D., Gao, T. & Bazant, M. Z. Modeling the Metal–Insulator Phase Transition in Li_xCoO_2 for Energy and Information Storage. *Adv. Funct. Mater.* **29**, 1902821 (2019).
10. Alkhadra, M. A. et al. Electrochemical Methods for Water Purification, Ion Separations, and Energy Conversion. *Chem. Rev.* **122**, 13547–13635 (2022).
11. Wu, L. et al. Lithium recovery using electrochemical technologies: Advances and challenges. *Water Res.* **221**, 118822 (2022).
12. Zhao, X. et al. Recent progress on key materials and technical approaches for electrochemical lithium extraction processes. *Desalination* **546**, 116189 (2023).
13. Sun, L. et al. Recent progress and future perspective on practical silicon anode-based lithium ion batteries. *Energy Storage Mater.* **46**, 482–502 (2022).
14. Zhang, Y. et al. Towards better Li metal anodes: Challenges and strategies. *Mater. Today* **33**, 56–74 (2020).
15. Zhao, H. et al. Cobalt-Free Cathode Materials: Families and their Prospects. *Adv. Energy Mater.* **12**, 2103894 (2022).
16. Hebert, A. & McCalla, E. The role of metal substitutions in the development of Li batteries, part I: cathodes. *Mater. Adv.* **2**, 3474–3518 (2021).
17. Padhi, A. K., Nanjundaswamy, K. S. & Goodenough, J. B. Phospho-olivines as Positive-Electrode Materials for Rechargeable Lithium Batteries. *J. Electrochem. Soc.* **144**, 1188–1194 (1997).
18. Wang, M. et al. Recycling of lithium iron phosphate batteries: Status, technologies, challenges, and prospects. *Renew. Sustain. Energy Rev.* **163**, 112515 (2022).
19. Tolganbek, N., Yerkinbekova, Y., Kalybekkyzy, S., Bakenov, Z. & Mentbayeva, A. Current state of high voltage olivine structured $LiMPO_4$ cathode materials for energy storage applications: A review. *J. Alloy. Compd.* **882**, 160774 (2021).
20. Wani, T. A. & Suresh, G. A comprehensive review of $LiMnPO_4$ based cathode materials for lithium-ion batteries: current strategies to improve its performance. *J. Energy Storage* **44**, 103307 (2021).
21. Mauger, A. & Julien, C. Olivine Positive Electrodes for Li-Ion Batteries: Status and Perspectives. *Batteries* **4**, 39 (2018).
22. Deng, Y. et al. Recent Advances of Mn-Rich $LiFe_{1-y}Mn_yPO_4$ ($0.5 \leq y < 1.0$) Cathode Materials for High Energy Density Lithium Ion Batteries. *Adv. Energy Mater.* **7**, 1601958 (2017).
23. Yang, L. et al. Olivine $LiMn_xFe_{1-x}PO_4$ cathode materials for lithium ion batteries: restricted factors of rate performances. *J. Mater. Chem. A* **9**, 14214–14232 (2021).
24. Zhang, M., Garcia-Araez, N. & Hector, A. L. Understanding and development of olivine $LiCoPO_4$ cathode materials for lithium-ion batteries. *J. Mater. Chem. A* **6**, 14483–14517 (2018).
25. Li, Y. & Taniguchi, I. Synthesis of $LiNi_{1-x}Co_xPO_4$/C nanocomposite cathode for lithium ion batteries by a combination of aerosol and powder technologies. *Adv. Powder Technol.* **30**, 180–189 (2019).
26. Bramnik, N. N., Trots, D. M., Hofmann, H. J. & Ehrenberg, H. Mixed $LiCo_{0.6}M_{0.4}PO_4$ (M = Mn, Fe, Ni) phosphates: cycling mechanism and thermal stability. *Phys. Chem. Chem. Phys.* **11**, 3271 (2009).
27. Mauger, A., Julien, C. M., Armand, M., Goodenough, J. B. & Zaghib, K. Li(Ni,Co)PO$_4$ as cathode materials for lithium batteries: Will the dream come true? *Curr. Opin. Electrochem.* **6**, 63–69 (2017).
28. Palmer, M. G. et al. In situ phase behaviour of a high capacity $LiCoPO_4$ electrode during constant or pulsed charge of a lithium cell. *Chem. Commun.* **52**, 14169–14172 (2016).
29. Strobridge, F. C. et al. Unraveling the Complex Delithiation Mechanisms of Olivine-Type Cathode Materials, $LiFe_xCo_{1-x}PO_4$. *Chem. Mater.* **28**, 3676–3690 (2016).
30. Muñoz-García, A. B. et al. Structural evolution of disordered $LiCo_{1/3}Fe_{1/3}Mn_{1/3}PO_4$ in lithium batteries uncovered. *J. Mater. Chem. A* **8**, 19641–19653 (2020).

31. Timrov, I., Aquilante, F., Cococcioni, M. & Marzari, N. Accurate electronic properties and intercalation voltages of olivine-type Li-ion cathode materials from extended Hubbard functionals. *PRX Energy* **1**, 033003 (2022).

32. Snydacker, D. H. & Wolverton, C. Transition-Metal Mixing and Redox Potentials in Li$_x$ (M$_{1-y}$ M′$_y$)PO$_4$ (M, M′ = Mn, Fe, Ni) Olivine Materials from First-Principles Calculations. *J. Phys. Chem. C.* **120**, 5932–5939 (2016).

33. Malik, R., Zhou, F. & Ceder, G. Phase diagram and electrochemical properties of mixed olivines from first-principles calculations. *Phys. Rev. B* **79**, 214201 (2009).

34. Bazant, M. Z. Theory of Chemical Kinetics and Charge Transfer based on Nonequilibrium Thermodynamics. *Acc. Chem. Res.* **46**, 1144–1160 (2013).

35. Wang, Q. et al. Application of phase-field method in rechargeable batteries. *Npj Comput. Mater.* **6**, 176 (2020).

36. Birkholz, O. & Kamlah, M. Electrochemical Modeling of Hierarchically Structured Lithium-Ion Battery Electrodes. *Energy Technol.* **9**, 2000910 (2021).

37. Liu, K. et al. Electrochemical modeling and parameterization towards control-oriented management of lithium-ion batteries. *Control Eng. Pract.* **124**, 105176 (2022).

38. Zhao, H. *Data-driven Modeling of Lithium Intercalation Materials*. (Massachusetts Institute of Technology, 2021).

39. Nguyen, T.-T. et al. Mathematical Modeling of Energy-Dense NMC Electrodes: I. Determination of Input Parameters. *J. Electrochem. Soc.* **169**, 040546 (2022).

40. Smith, R. B., Khoo, E. & Bazant, M. Z. Intercalation Kinetics in Multiphase-Layered Materials. *J. Phys. Chem. C.* **121**, 12505–12523 (2017).

41. Cogswell, D. A. & Bazant, M. Z. Coherency Strain and the Kinetics of Phase Separation in LiFePO$_4$ Nanoparticles. *ACS Nano* **6**, 2215–2225 (2012).

42. Li, Y. et al. Fluid-enhanced surface diffusion controls intraparticle phase transformations. *Nat. Mater.* **17**, 915–922 (2018).

43. Ferguson, T. R. & Bazant, M. Z. Nonequilibrium Thermodynamics of Porous Electrodes. *J. Electrochem. Soc.* **159**, A1967–A1985 (2012).

44. Bai, P., Cogswell, D. A. & Bazant, M. Z. Suppression of Phase Separation in LiFePO$_4$ Nanoparticles During Battery Discharge. *Nano Lett.* **11**, 4890–4896 (2011).

45. de Klerk, N. J. J., Vasileiadis, A., Smith, R. B., Bazant, M. Z. & Wagemaker, M. Explaining key properties of lithiation in TiO2 -anatase Li-ion battery electrodes using phase-field modeling. *Phys. Rev. Mater.* **1**, 025404 (2017).

46. Vasileiadis, A. et al. Toward Optimal Performance and In-Depth Understanding of Spinel Li$_4$Ti$_5$O$_{12}$ Electrodes through Phase Field Modeling. *Adv. Funct. Mater.* **28**, 1705992 (2018).

47. Agrawal, S. & Bai, P. Dynamic interplay between phase transformation instabilities and reaction heterogeneities in particulate intercalation electrodes. *Cell Rep. Phys. Sci.* **3**, 100854 (2022).

48. Smith, R. B. & Bazant, M. Z. Multiphase Porous Electrode Theory. *J. Electrochem. Soc.* **164**, E3291–E3310 (2017).

49. Ferguson, T. R. & Bazant, M. Z. Phase Transformation Dynamics in Porous Battery Electrodes. *Electrochim. Acta* **146**, 89–97 (2014).

50. Zhao, H. & Bazant, M. Z. Population dynamics of driven autocatalytic reactive mixtures. *Phys. Rev. E* **100**, 012144 (2019).

51. Dreyer, W., Guhlke, C. & Huth, R. The behavior of a many-particle electrode in a lithium-ion battery. *Phys. Nonlinear Phenom.* **240**, 1008–1019 (2011).

52. Bazant, M. Z. Thermodynamic stability of driven open systems and control of phase separation by electro-autocatalysis. *Faraday Discuss* **199**, 423–463 (2017).

53. Bai, P. & Tian, G. Statistical kinetics of phase-transforming nanoparticles in LiFePO$_4$ porous electrodes. *Electrochim. Acta* **89**, 644–651 (2013).

54. Park, J. et al. Fictitious phase separation in Li layered oxides driven by electro-autocatalysis. *Nat. Mater.* **20**, 991–999 (2021).

55. Cahn, J. W. & Hilliard, J. E. Free Energy of a Nonuniform System. I. Interfacial Free Energy. *J. Chem. Phys.* **28**, 258 (1958).

56. Cahn, J. W. & Hilliard, J. E. Free Energy of a Nonuniform System. III. Nucleation in a Two-Component Incompressible Fluid. *J. Chem. Phys.* **31**, 688–699 (1959).

57. Cahn, J. W. & Hilliard, J. E. Spinodal decomposition: A reprise. *Acta Met.* **19**, 151–161 (1971).

58. Binder, K. Theory of first-order phase transitions. *Rep. Prog. Phys.* **50**, 783–859 (1987).

59. Daubner, S. et al. Multiphase-field modeling of spinodal decomposition during intercalation in an Allen-Cahn framework. *Phys. Rev. Mater.* **5**, 035406 (2021).

60. Zeng, Y. & Bazant, M. Z. Cahn-Hilliard Reaction Model for Isotropic Li-ion Battery Particles. *MRS Proc.* **1542**, mrss13-1542-g02-01 (2013).

61. Lee, D. et al. Physical, mathematical, and numerical derivations of the Cahn–Hilliard equation. *Comput. Mater. Sci.* **81**, 216–225 (2014).

62. Chandesris, M., Caliste, D., Jamet, D. & Pochet, P. Thermodynamics and Related Kinetics of Staging in Intercalation Compounds. *J. Phys. Chem. C.* **123**, 23711–23720 (2019).

63. Rykner, M. & Chandesris, M. Free Energy Model for Lithium Intercalation in Graphite: Focusing on the Coupling with Graphene Stacking Sequence. *J. Phys. Chem. C.* **126**, 5457–5472 (2022).

64. Di Leo, C. V., Rejovitzky, E. & Anand, L. A Cahn–Hilliard-type phase-field theory for species diffusion coupled with large elastic deformations: Application to phase-separating Li-ion electrode materials. *J. Mech. Phys. Solids* **70**, 1–29 (2014).

65. Afshar, A. & Di Leo, C. V. A thermodynamically consistent gradient theory for diffusion–reaction–deformation in solids: Application to conversion-type electrodes. *J. Mech. Phys. Solids* **151**, 104368 (2021).

66. Zhang, X., Shyy, W. & Marie Sastry, A. Numerical Simulation of Intercalation-Induced Stress in Li-Ion Battery Electrode Particles. *J. Electrochem. Soc.* **154**, A910 (2007).

67. Castelli, G. F., von Kolzenberg, L., Horstmann, B., Latz, A. & Dörfler, W. Efficient Simulation of Chemical–Mechanical Coupling in Battery Active Particles. *Energy Technol.* **9**, 2000835 (2021).

68. Daubner, S., Weichel, M., Schneider, D. & Nestler, B. Modeling intercalation in cathode materials with phase-field methods: Assumptions and implications using the example of Li FePO$_4$. *Electrochim. Acta* **421**, 140516 (2022).

69. Bazant, M. et al. *Learning heterogeneous reaction kinetics from X-ray movies pixel-by-pixel.* https://www.researchsquare.com/article/rs-2320040/v1 (2022).

70. Fraggedakis, D. et al. Theory of coupled ion-electron transfer kinetics. *Electrochim. Acta* **367**, 137432 (2021).

71. Galuppini, G. et al. Efficient computation of safe, fast charging protocols for multiphase lithium-ion batteries: A lithium iron phosphate case study. *J. Power Sources* **580**, 233272 (2023).

72. Piazza, R. *Statistical Physics: A Prelude and Fugue for Engineers*. (Springer International Publishing, 2017).

73. Han, B. C., Van der Ven, A., Morgan, D. & Ceder, G. Electrochemical modeling of intercalation processes with phase field models. *Electrochim. Acta* **49**, 4691–4699 (2004).

74. Tardif, S. et al. Combining *operando* X-ray experiments and modelling to understand the heterogeneous lithiation of graphite electrodes. *J. Mater. Chem. A* **9**, 4281–4290 (2021).

75. Hörmann, N. G. & Groß, A. Phase field parameters for battery compounds from first-principles calculations. *Phys. Rev. Mater.* **3**, 055401 (2019).

76. Dreyer, W. et al. The thermodynamic origin of hysteresis in insertion batteries. *Nat. Mater.* **9**, 448–453 (2010).

77. Hillert, M. The compound energy formalism. *J. Alloy. Compd.* **320**, 161–176 (2001).

78. Saunders, N. & Miodownik, A. P. *CALPHAD: Calculation of Phase Diagrams - A Comprehensive Guide*. vol. 1 (Elsevier, 1998).

79. Hillert, M. Some properties of the compound energy model. *Calphad* **20**, 333–341 (1996).

80. Phan, A. T., Gheribi, A. E. & Chartrand, P. Modelling of phase equilibria of LiFePO$_4$-FePO$_4$ olivine join for cathode material. *Can. J. Chem. Eng.* **97**, 2224–2233 (2019).

81. Kobayashi, G. et al. Shift of redox potential and kinetics in Li$_x$(Mn$_y$Fe1−y)PO$_4$. *J. Power Sources* **189**, 397–401 (2009).

82. Jalkanen, K. & Karppinen, M. Electrochemical Performance and Delithiation/Lithiation Characteristics of Mixed LiFe$_{1-y}$M$_y$PO$_4$ (M = Co, Ni) Electrode Materials. *J. Electrochem. Soc.* **162**, A2780–A2788 (2015).

83. Ravnsbæk, D. B. et al. Extended Solid Solutions and Coherent Transformations in Nanoscale Olivine Cathodes. *Nano Lett.* **14**, 1484–1491 (2014).

84. Ravnsbæk, D. B. et al. Engineering the Transformation Strain in LiMn$_y$Fe$_{1-y}$PO$_4$ Olivines for Ultrahigh Rate Battery Cathodes. *Nano Lett.* **16**, 2375–2380 (2016).

85. Ravnsbaek, D. B. et al. In-Situ Study of Electrochemically-Driven Phase Transitions in LiMn$_y$Fe$_{1-y}$PO$_4$. *ECS Meet. Abstr.* **MA2013-02**, 255–255 (2013).

86. Cogswell, D. A. & Bazant, M. Z. Size-dependent phase morphologies in LiFePO$_4$ battery particles. *Electrochem. Commun.* **95**, 33–37 (2018).

87. Zhong, Y. et al. Microwave-assisted rheological phase synthesis of LiFe $_{0.5}$Mn $_{0.3}$Co$_{0.2}$PO$_4$/C cathode materials for lithium ion batteries. *Mater. Res. Express* **6**, 035003 (2018).

88. Nwachukwu, I. M., Nwanya, A. C., Ekwealor, A. B. C. & Ezema, F. I. Recent progress in Mn and Fe-rich cathode materials used in Li-ion batteries. *J. Energy Storage* **54**, 105248 (2022).

89. Xie, Y., Yu, H.-T., Yi, T.-F. & Zhu, Y.-R. Understanding the Thermal and Mechanical Stabilities of Olivine-Type LiMPO$_4$ (M = Fe, Mn) as Cathode Materials for Rechargeable Lithium Batteries from First Principles. *ACS Appl. Mater. Interfac.* **6**, 4033–4042 (2014).

90. Lethole, N. L., Ngoepe, P. E. & Chauke, H. R. First-principles study: Effect of lithium and sodium intercalation in transition metal phosphates, MPO4 (M: Mn, Fe, Co). *Comput. Condens. Matter* **22**, e00437 (2020).

91. Hashambhoy, A. M. & Whitacre, J. F. Li Diffusivity and Phase Change in LiFe0.5Mn0.5PO4: AComparative Study using Galvanostatic Intermittent Titrationand Cyclic Voltammetry. *J. Electrochem. Soc.* **158**, A390 (2011).

92. Fuller, T. F., Doyle, M. & Newman, J. Simulation and Optimization of the Dual Lithium Ion Insertion Cell. *J. Electrochem. Soc.* **141**, 1–10 (1994).

93. Katrašnik, T. et al. Entering Voltage Hysteresis in Phase-Separating Materials: Revealing the Electrochemical Signature of the Intraparticle Phase-Separated State. *Adv. Mater.* **35**, 2210937 (2023).

94. Li, Y. et al. Current-induced transition from particle-by-particle to concurrent intercalation in phase-separating battery electrodes. *Nat. Mater.* **13**, 1149–1156 (2014).

95. Liu, H. et al. Capturing metastable structures during high-rate cycling of LiFePO$_4$ nanoparticle electrodes. *Science* **344**, 1252817 (2014).

96. Levi, M. D. et al. Collective Phase Transition Dynamics in Microarray Composite Li$_x$FePO$_4$ Electrodes Tracked by in Situ Electrochemical Quartz Crystal Admittance. *J. Phys. Chem. C.* **117**, 15505–15514 (2013).

97. Yamanaka, T. et al. Evolution and Migration of Lithium-Deficient Phases during Electrochemical Delithiation of Large Single Crystals of LiFePO$_4$. *ACS Appl. Energy Mater.* **1**, 1140–1145 (2018).

98. Koyama, Y. et al. Hidden Two-Step Phase Transition and Competing Reaction Pathways in LiFePO$_4$. *Chem. Mater.* **29**, 2855–2863 (2017).

99. Sharma, N., Yu, D. H., Zhu, Y., Wu, Y. & Peterson, V. K. In operando neutron diffraction study of the temperature and current rate-dependent phase evolution of LiFePO$_4$ in a commercial battery. *J. Power Sources* **342**, 562–569 (2017).

100. Delmas, C., Maccario, M., Croguennec, L., Le Cras, F. & Weill, F. Lithium deintercalation in LiFePO4 nanoparticles via a domino-cascade model. *Nat. Mater.* **7**, 665–671 (2008).

101. Zhang, X. et al. Rate-Induced Solubility and Suppression of the First-Order Phase Transition in Olivine LiFePO$_4$. *Nano Lett.* **14**, 2279–2285 (2014).

102. Zhou, F., Maxisch, T. & Ceder, G. Configurational Electronic Entropy and the Phase Diagram of Mixed-Valence Oxides: The Case of Li x FePO4. *Phys. Rev. Lett.* **97**, 155704 (2006).

103. Delacourt, C., Poizot, P., Tarascon, J.-M. & Masquelier, C. The existence of a temperature-driven solid solution in LixFePO$_4$ for $0 \le x \le 1$. *Nat. Mater.* **4**, 254–260 (2005).

104. Cogswell, D. A. & Bazant, M. Z. Theory of Coherent Nucleation in Phase-Separating Nanoparticles. *Nano Lett.* **13**, 3036–3041 (2013).

105. Verhallen, T. W., Lv, S. & Wagemaker, M. Operando Neutron Depth Profiling to Determine the Spatial Distribution of Li in Li-ion Batteries. *Front. Energy Res.* **6**, 62 (2018).

106. Zhang, X. In operando phase transition and lithium ion transportation in LiFePO$_4$. (Doctoral dissertation TU Delft, 2015).

107. Azimi, V., Allam, A. & Onori, S. Extending Life of Lithium-Ion Battery Systems by Embracing Heterogeneities via an Optimal Control-Based Active Balancing Strategy. *IEEE Trans. Control Syst. Technol.* **31**, 1235–1249 (2023).

AUTHOR CONTRIBUTIONS
P.O. developed the code and analyzed the results. P.O., M.W., A.V. conceived and designed the project. P.O. and A.V. led the collaboration. A.V. supervised the work. All the authors wrote, contributed and discussed the final paper.

COMPETING INTERESTS
The authors declare no competing interests.

ADDITIONAL INFORMATION
Supplementary information The online version contains supplementary material available at https://doi.org/10.1038/s41524-023-01109-1.

Correspondence and requests for materials should be addressed to Alexandros Vasileiadis.

Reprints and permission information is available at http://www.nature.com/reprints

Publisher's note Springer Nature remains neutral with regard to jurisdictional claims in published maps and institutional affiliations.